

High Temperature Fatigue Performance of Electron Beam Powder Bed Fusion Manufactured Alloy 718



HENRIK KJELLSSON, ARUN RAMANATHAN BALACHANDRAMURTHI, JOHAN MOVERARE, and THOMAS HANSSON

The microstructure and mechanical properties of additively manufactured (AM) parts have been shown to be different from that of cast and wrought counterparts. In this study, electron beam powder bed fusion (EB-PBF) fabricated Alloy 718 was exposed to three different heat treatment routes followed by strain-controlled fatigue testing at 550 °C. The fatigue tests were performed with specimens built with their center axis parallel and transverse relative to the build direction. The microstructure showed saturated precipitation of δ -Ni₃Nb after repeated solution treatment at 954 °C. In contrast, no δ -Ni₃Nb precipitates could be observed after a single-step solution treatment at 1025 °C. However, the disparity of secondary phases showed no noticeable influence on the fatigue life. A significant difference in fatigue behavior was noted between the parallel and transverse directions. The specimens loaded parallel to the elongated grains showed on average $\sim 5\times$ greater life in comparison to the perpendicularly loaded specimens. Compared to corresponding heat-treated material conditions tested at ambient temperature, the specimens showed lower life at high strain amplitude and superior life at low strain amplitude. Moreover, competitive internal and surface failure modes were observed at the lower strain amplitudes while for the higher strain ranges, surface failure modes dominated.

<https://doi.org/10.1007/s11661-022-06681-7>
© The Author(s) 2022

I. INTRODUCTION

ADDITIVE manufacturing (AM) has shown to offer several advantages over conventional manufacturing techniques in various aspects, such as material efficiency, design complexity, and production flexibility. In the next few years, the technology is likely to be extensively used within industrial production. There are already several commercialized systems available for AM of metallic materials on the market.^[1] Two of the major AM techniques used extensively in critical applications, such as aerospace, power are directed energy deposition (DED) and powder bed fusion (PBF). While DED has shown to be beneficial for repair and cladding applications,^[2] the greater design freedom of powder bed-based

AM systems allows for the fabrication of parts with improved strength-to-weight ratio.^[3,4] These appealing characteristics of AM have captured the attention of the aerospace industry due to the opportunity of increased material utilization and production of lightweight components.^[5] The growing interest of AM Alloy 718 has also drawn academic attention by a steadily increasing number of publications on AM of Alloy 718 in recent years.^[6]

Alloy 718 is considered to be the workhorse among superalloys for aerospace applications. One advantage is the relatively high iron content in the matrix, making it less expensive compared to superalloys with higher nickel composition.^[7] Alloy 718 is thermally stable up to 650 °C and, therefore, is commonly used for structural components in the hot sections of gas turbines. The alloy is primarily strengthened by adding niobium to form BCT γ'' -Ni₃Nb precipitates. In addition, the alloy also has a lower volume fraction of γ' -Ni₃(Al, Ti) precipitates which contributes to the strengthening. The volume fraction ratio of γ'' to γ' is approximately 3:1 where the γ'' precipitates generate about seven times higher relative lattice misfits compared with the γ' precipitates.^[8] Hence, the precipitation of γ'' is more sluggish compared to γ' . The metastable nature of γ'' makes the alloy susceptible to form incoherent δ -Ni₃Nb in temperature ranges of ~ 700 to 980 °C. The morphology of the δ phase is incoherent with the matrix and

HENRIK KJELLSSON and ARUN RAMANATHAN BALACHANDRAMURTHI are with the Department of Engineering Science, University West, 46186, Trollhättan, Sweden. JOHAN MOVERARE is with the Department of Engineering Science, University West and also with the Department of Management and Engineering, Linköping University, 58183, Linköping, Sweden. THOMAS HANSSON is with the Department of Engineering Science, University West and also with the GKN Aerospace Sweden AB, 46181, Trollhättan, Sweden. Contact e-mail: thomas.hansson@hv.se.

Manuscript submitted November 21, 2021; accepted March 30, 2022.

Article published online April 29, 2022

does not contribute towards a direct strengthening of the alloy. In addition, with an increased volume fraction of δ phase, the Nb content in the matrix becomes depleted, which hinders the precipitation of strengthening γ'' . However, low fractions of plate-like δ phase along the grain boundaries have shown to result in grain boundary pinning and improved creep properties.^[9] In addition, Alloy 718 tends to form Laves phase due to the segregation Nb during solidification. Laves is a topologically close-packed phase, which is detrimental because of its brittle nature in combination with low melting point and compositional segregation of Nb content.^[10] However, suitable thermal post-processing has proven to result in homogenization and dissolution of Laves phase in the matrix.^[11] The ability to preserve high strength at elevated temperature and low thermal conductivity make Alloy 718 difficult to process by conventional machining methods.^[12] Hence, traditional manufacturing techniques entails rapid tool wear and high machining cost.

AM is showing potential to replace several applications in the manufacturing industry where previously only conventional material processing techniques were possible. One of the powder-based AM methods capable of processing Alloy 718 is electron beam powder bed fusion (EB-PBF). The process was developed and commercialized by the Swedish company Arcam AB. The system was patented in 1997, and the first commercial model was launched in 2002.^[13] The process takes place in a vacuum chamber at an elevated temperature and starts with a thin layer of metal powder spread on a build platform using a rake. Thereafter, an electron beam sweeps across the layer several times until the powder is slightly sintered. Sequentially, the electron beam is focused to fuse the powder according to the sliced section pattern of a CAD model. Next, the platform is lowered, and a new layer of powder is applied on top of the solidified layer. This scheme is repeated until all section layers of the CAD model are built from the bottom and upwards.^[14,15] The use of an electron beam as an energy source provides higher total power and enables higher scan speed compared to laser beam systems.^[16] In addition, the elevated chamber temperature and layer-wise preheating result in a higher processing temperature, and consequently, lesser residual stresses are induced in the part.

There has already been a lot of work published on understanding the processing of Alloy 718 by EB-PBF and the resulting microstructure.^[17–24] Moreover, the effect of various thermal post-treatments on material densification and precipitation strengthening has widely been investigated.^[23,25,26] In addition, a number of studies have been performed on the tensile properties at room^[26–28] and elevated^[21,25,29] temperatures. Deng *et al.*^[23] showed anisotropic tensile properties of the build due to texture, elongated grains, and distribution of defects. Columnar grains elongated parallel to the build direction with strong $\langle 001 \rangle$ texture have extensively been reported in EB-PBF Alloy 718.^[23,25,26] Furthermore, conventionally conducted post-treatments shows a limited effect on the grain morphology.^[26,28,30] Consequently, the anisotropic mechanical properties

stay inherent in the built part. It is worth noting that the solidification structure and texture are not unique to EB-PBF^[31] and can be controlled by adapting the process parameters.

The fatigue performance of EB-PBF Alloy 718 has previously been studied,^[26,27,32,33] and few experiments have been focusing on the low cycle fatigue (LCF) performance.^[30,34,35] Balachandramurthi *et al.*^[35] studied the LCF behavior of Alloy 718 at room temperature and showed that the anisotropic fatigue properties closely correlate to the anisotropy of Young's modulus. However, research has focused more on the fatigue properties at room temperature rather than common service temperatures for Alloy 718. Deng *et al.*^[33] investigated dwell-fatigue crack propagation and found varying crack resistance dependent on load direction with respect to the grain orientation at 550 °C. Kirka *et al.*^[34] studied the LCF behavior of EB-PBF Alloy 718 °C at 650 °C and investigated the effect of grain morphology on crack propagation. The results showed that while loaded parallel to the build direction failure was transgranular, whereas it was intergranular when loaded transverse to the build direction in the case of columnar grain structure.

While the anisotropic fatigue behavior of Alloy 718 processed by EB-PBF previously has been studied at high temperatures,^[33,34] the influence of commonly conducted heat treatments for AM built Alloy 718 has not yet been reported. This study seeks to investigate the effect of various post-processing routes on the phase constitution, and ultimately, the influence on fatigue behavior of EB-PBF fabricated Alloy 718 at 550 °C. For this objective, the alloy was examined in three different thermal post-treatment conditions. In addition, the fatigue tests were performed in two different orientations with respect to the build direction to study the anisotropic mechanical properties of the build. Finally, a comprehensive fracture analysis was conducted to evaluate the influence of crack initiation mode on fatigue performance.

II. EXPERIMENTAL PROCEDURE

An Arcam A2X Electron Beam Melting (EBM) system was employed to manufacture the fatigue specimens. The feedstock was gas atomized Alloy 718 powder with the size range of 45–106 μm with chemical composition as listed in Table I. The EBM system was run with EBM Control software V4.2.7 using Arcam heat model algorithm for beam current and velocity control, Inco 4.2.76 theme as raster scan strategy, and speed function 63 settings. Four build cycles containing ten cylindrical and two rectangular cuboid blanks each were fabricated with the nominal geometries as illustrated in Figure 1(a). The build platform of stainless steel was pre-heated to 1025 °C before each build started. Each of the sequentially applied powder layers was pre-heated to maintain a high building temperature and slightly sinter the powder before melting the layer. All build cycles applied a scan strategy of 90° rotation of

each layer, 75 μm layer thickness, and 125 μm hatch spacing.

A. Post-treatments

All blanks designated for fatigue testing were subjected to thermal post-treatment. However, few of the fabricated blanks were left in the as-built condition as assessment references. All fatigue test blanks were exposed to the same hot isostatic pressing (HIP) treatment using a Quintus Technologies QIH-21 HIP unit followed by uniformed rapid cooling in accordance with ASTM F3055.^[36] Thereafter, the HIPed blanks were divided into three groups and exposed to different solution treatment and aging (STA) heat treatments which henceforth will be referred to as standard (STD), repair (REP), or single-step solution (SSS) heat treatment (HT). All solution and aging steps were conducted in a vacuum furnace followed by air cooling with a rate not less than 20 $^{\circ}\text{C}/\text{min}$, except for the transition between the first and second age-hardening step in the STD and REP treatments. There, the cooling was conducted using furnace cooling with a cooling rate of

55 $^{\circ}\text{C}/\text{h}$. The thermal histories of the blanks are illustrated in Figure 2 with the specific time and temperature listed in Table II. The motivation for the HT parameters was established in a previous study,^[35] where the SSS cycle is selected as representative heat treatment for Alloy 718 components used for oil and gas industry application, and the REP heat treatment is a simulation of multiple repair welding cycles.

All blanks were machined into cylindrical fatigue specimens following the ASTM E606/E606M^[37] standard with the specimen geometries specified in Figure 1(b). The cylindrical blanks were machined into fatigue specimens with their center axis parallel to the build direction. In contrast, the rectangular cuboid blanks were sectioned into six square cuboids and then machined into fatigue specimens with their center axis perpendicular to the build direction, as illustrated in Figure 1(a). Specimens machined with the center axis parallel and perpendicular with respect to the build direction will henceforth be referred to as vertical and horizontal specimens, respectively. All the test specimens were low stress ground and polished longitudinally such that the polishing tracks are parallel to the loading axis of the specimens.

Table I. Nominal Chemical Composition of Alloy 718 Powder

Element	Wt Pct
Carbon	0.05
Chromium	18.70
Molybdenum	3.00
Niobium	5.14
Titanium	0.94
Aluminum	0.42
Iron	18.00
Nickel	53.30

B. Mechanical Testing

Uniaxial strain-controlled fatigue tests were performed following ASTM E606/E606M^[37] by employing an MTS servohydraulic load frame with a maximum load capacity of 160 kN. The test system was equipped with an Instron 8800 control system running LCF3 software. An Instron model 2632-54 high-temperature axial extensometer with a 12.5 mm gauge length was used for strain measurement. An MTS model 652.01 high-temperature furnace configured with three temperature zones, equipped with a model 409.81 temperature

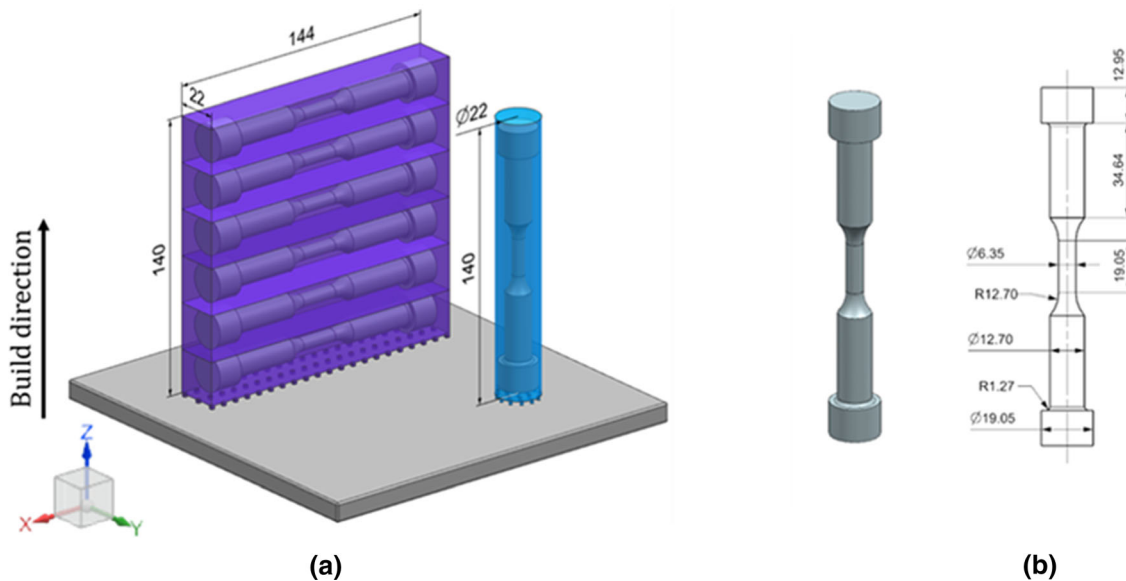


Fig. 1—CAD models of (a) blanks with illustration of fatigue specimen orientations and (b) fatigue specimen geometry. All dimensions are in millimeters (mm).

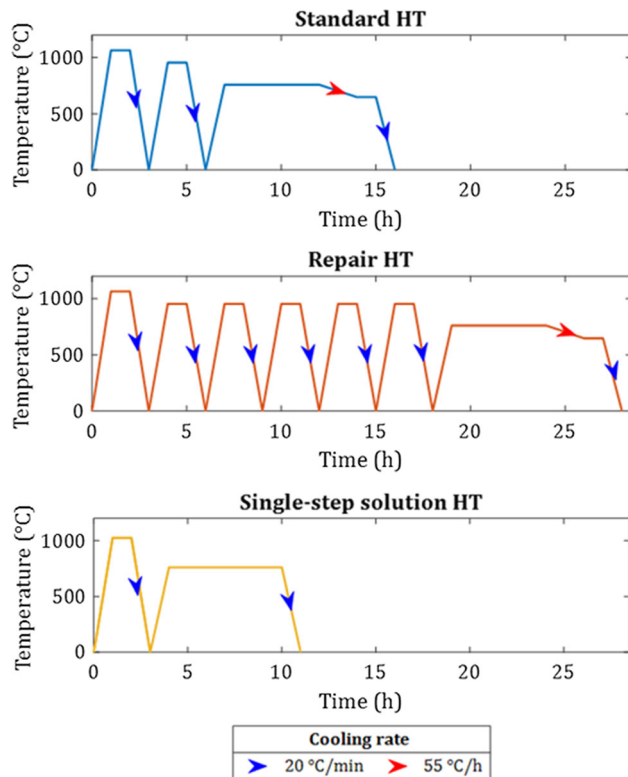


Fig. 2—Graphs showing the thermal history for specimens exposed to STD, REP, and SSS heat treatments.

controller was employed for temperature control. The test was conducted at 550 °C using a strain ratio of $R\epsilon=0$ with a constant frequency of 0.5 Hz, following a triangular waveform. The frequency was increased to 5.0 Hz after 43,200 cycles if the plastic strain had not exceeded 0.01 pct. When the frequency was increased, the control mode was also switched to load control using the same stress response as displayed prior to the switch. The test end criterion was predetermined as a 20 pct drop in the peak load from that of the stabilized hysteresis loop. Thereafter, a tensile load was applied to fracture the specimen and to reveal the fracture surfaces. The two specimen orientations were tested at seven strain ranges, varying from 0.5 to 2.0 pct. A similar test procedure was conducted to investigate the LCF behavior of EB-PBF fabricated Alloy 718 at room temperature in a previous study.^[35]

C. Metallography and Fractography

Fractography was performed by employing an Olympus SZX9 stereo microscope and a Zeiss EVO 50 scanning electron microscope (SEM) equipped with an Oxford X-Max^N 20 mm² energy-dispersive X-ray spectroscopy (EDS) detector.

For metallographic analysis, samples were prepared by precision cutting, hot mounting, grinding, and polishing to a 3 μm diamond suspension finish. The as-polished surface was investigated employing an Olympus BX60M light optical microscope (LOM).

Defect fraction quantification was performed by acquiring 20 image fields of $\times 50$ magnification from two samples in each material condition. The 20 image field from the two cross-sections then corresponds to an area of approximately 48.3 mm².

The polished samples were electrolytically etched using oxalic acid at 3 V. The etched microstructure was investigated using a Zeiss AX10 LOM. Further high magnification analysis was performed using a Zeiss Gemini 450 field emission SEM. The width of the columnar grains was measured by acquiring 30 fields at $\times 100$ magnification in the x-y and x-z planes from three specimens in each HT condition. No significant difference in the width with respect to the columnar diameter was noted between the x-y and x-z planes. Therefore, a total of 180 image fields from both planes was used for width measurement by applying the linear intercept method. However, the height of the grains was only evaluated from the 90 images in the x-z plane.

Thin foils of the specimens from the direction parallel to the build direction were prepared for transmission electron microscopy (TEM). To obtain the thin films, the specimens were firstly ground to a thickness of around 100 μm . 3 mm diameter discs were punched out from these specimens and were further ground to a thickness of approximately 20 μm by a Gatan 656 dimple grinder. A Gatan 691 ion beam milling instrument was then used to obtain transparent thin films suitable for TEM. The thin films were characterized using a 200X Thermo Scientific Talos Arctica TEM operating at an accelerating voltage of 200 kV. The size of the precipitates was estimated by an image analysis technique based on the TEM images. For each sample, five dark-field TEM images in the same height from the top and bottom of the samples were taken, and for each image, approximately 20 precipitates were considered enabling proper estimation of the length of the γ'' precipitates. All image analysis techniques were performed using open-source ImageJ image processing software.

III. RESULTS AND DISCUSSION

Since the test specimens were subjected to machining, neither the characteristics of the contour and transition region nor the microstructural gradient along the build direction will be addressed in this paper. Previous studies^[18,21,38] have already investigated the microstructural gradient of EB-PBF Alloy 718. Moreover, discussion on the characteristics of the contour and transition region can be found elsewhere.^[23,26,31] Thus, only the microstructural characteristics and properties of the bulk region are discussed henceforth.

A. Defects

Figure 3 presents the cross-sections parallel to the build direction of the as-built (AB) and HIP + STA samples in as-polished conditions. The blanks in AB condition exhibited numerous agglomerated defects along the build direction in conjunction with highly

Table II. Parameters Used for Thermal Post-processing

HT	ST1	ST2	Age1	Age2
STD	1065 °C, 1 h	954 °C, 1 h	760 °C, 5 h	649 °C, 1 h
REP	1065 °C, 1 h	954 °C, 1 h (× 5)	760 °C, 5 h	649 °C, 1 h
SSS	1025 °C, 1 h	—	760 °C, 6 h	—

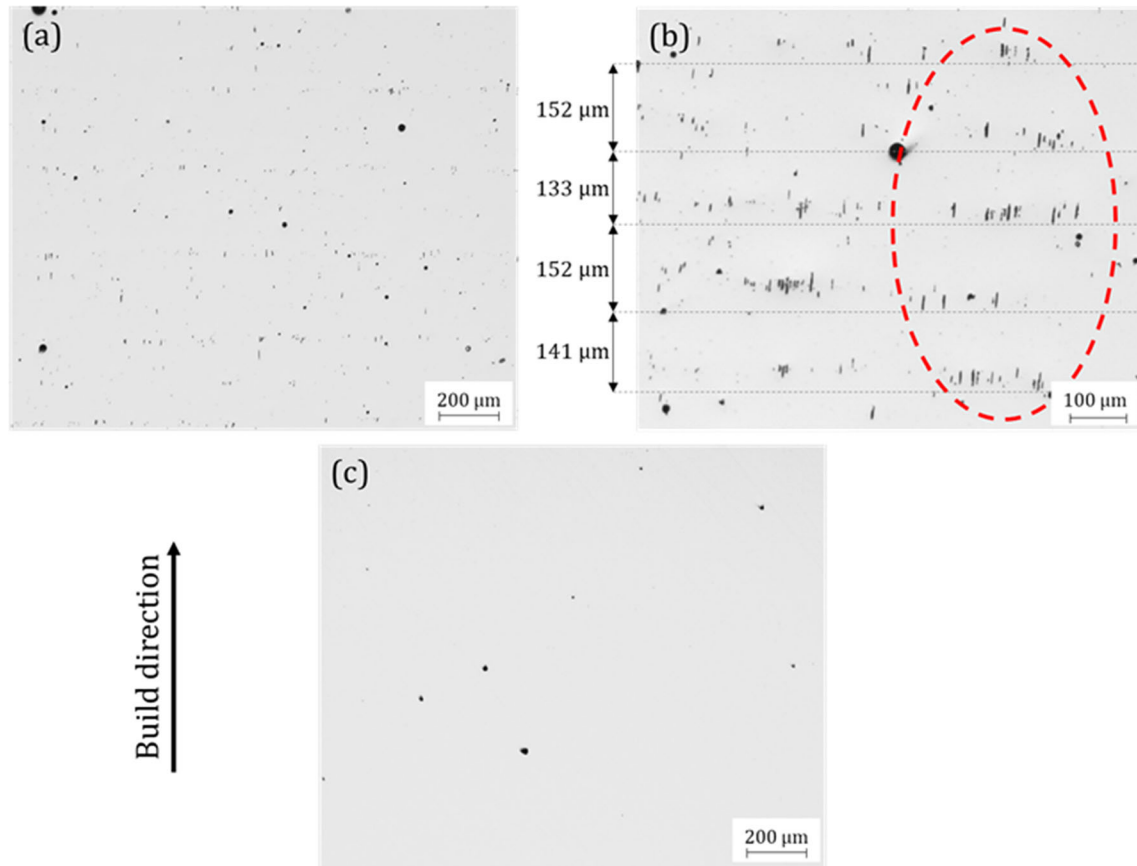


Fig. 3—LOM images of as-polished cross-sections showing (a) as-built condition, (b) shrinkage porosity in as-built condition, and (c) HIP + STA condition.

spherical defects with a more random size and distribution. The agglomerated defects showed a tendency of horizontal alignment parallel to the layers. Figure 3(b) shows a vertical defect spacing of approximately 150 μm , illustrated by the horizontal dashed lines.

As the arrays of agglomerated defects were distributed at a vertical spacing of approximately twice the layer thickness, and the scan direction was rotated by 90° in each layer, it was assumed that only every other array arrangement exposes at the cross-section. Therefore, indicate that the agglomerated defects most likely are shrinkage porosity. Such defects are attributed to inadequate energy input, causing insufficient accumulation of melt to accommodate the thermal contraction of the layer.^[24] Like lack-of-fusion (LoF) and gas pores, shrinkage pores are generally classified as internal defects. While gas pores are primarily related to the feedstocks manufacturing process, LoF and

shrinkage porosity are more associated with machine-related parameters. In contrast to LoF, shrinkage porosity occurs as a result of residual thermal stress generated during solidification, instead of insufficient bonding to the underlying layer or substrate. Balachandramurthi *et al.*^[26,32] proposed that the formation of shrinkage porosity is caused by the EBM systems heat model algorithm, which is programmed to maintain constant scan time for all raster scan passes. Thus, longer passes require higher scan speed which can only be obtained at the expense of heat input once the current capability is reached. After HIP + STA, the presence of agglomerated defects was significantly reduced, while the size of the spherical defects seemingly appeared relatively unaffected, see. Figure 3(c).

The spherical defects are well recognized as gas porosity and are commonly found in PBF fabricated parts. Figure 4(a) shows that all specimens exposed to

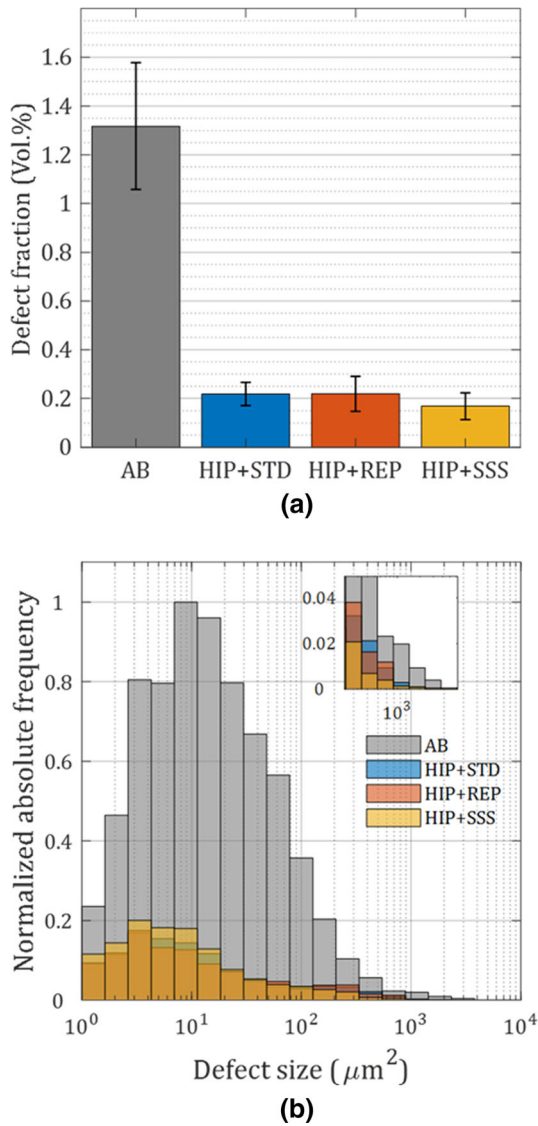


Fig. 4—Graphical representation of (a) defect volume fraction with 95 pct confidence interval and (b) defect size distribution before and after heat treatments. Note that the (b) histogram is represented with a logarithmic x -axis.

HIP + STA experienced substantial densification. However, Figure 4(b) indicates that the size range of the defects was marginally affected. The relatively unaffected size range is attributed to the limitation of HIP to permanently eliminate gas atoms of significantly larger radii relative to the lattice through diffusion. Furthermore, some gases are unable to diffuse because of insolubility in the matrix. Since the build is conducted in a vacuum chamber, the gas pores have most likely arisen from the feedstock powder. Previous studies have shown that the atomization process induces internal gas porosity of Alloy 718 powder.^[19] Chen *et al.*^[39] quantified the argon content for various atomization methods, which show that the entrapped porosity after HIP contains argon induced from the feedstock material. While the defect fraction was relatively similar after the different HT routes, Figure 4(b) indicates that the SSS HT specimens showed a slightly different distribution.

Remarkably, a higher fraction of defects $< \sim 18 \mu\text{m}^2$ and a lower fraction of defects $> \sim 130 \mu\text{m}^2$ were shown for the SSS HT specimens compared to the STD and REP HT ones. It has previously been highlighted that HIP is capable of compressing, although not diffuse, entrapped argon of EB-PBF fabricated Ti-6Al-4V.^[40,41] However, when the specimens are exposed to subsequent HT, the pores have been shown to re-expand. The re-expansion is attributed to increased internal pore pressure in conjunction with material softening during STA. Hence, the shift of average defect size and the slightly lower defect volume in the SSS condition could be attributed to less exposure time at elevated temperatures during the HT route. However, at a certain pore size, the internal pressure is not sufficient to further expand the pore significantly at the given temperature. Therefore, no further size distribution difference could be observed between the STD and REP HT. Note that these assumptions need to be interpreted with caution as some of the AB specimens showed a minor deviation of defect content which might have influenced the defect distribution. Also, it should be noted that some fraction of the residual cavities after HIP may be attributed to carbide pull-out during the sample preparation, which may have affected the result.

In addition, a minor fraction of randomly distributed irregular-shaped defects was observed in both AB and HIP + STA conditions. The lesser fraction of irregular-shaped defects presented in the AB and HIP + STA condition is attributed to processing-related LoF defects. While processing-related defects such as shrinkage porosity and LoF generally close during HIP, studies^[26,32] have shown that some LoF defects contain inclusions that prevent defects from fully healing. Thus, the remaining irregular-shaped defects found after HIP are presumably residual inclusions from LoF defects. Further analysis of the defects found that several of the inclusion consisted of non-metallic aluminum oxides, which are discussed more in section 3.4.

B. Microstructure

1. As-built

The AB specimens showed a columnar grain morphology with the grains elongated along the build direction. In contrast, the grains appeared equiaxed in the x - y plane. Columnar grain structures by epitaxial growth are commonly found in PBF fabricated parts when utilizing standard process parameters. The grain formation is ascribed to general high energy, scan speed, and scan strategy, applied to maximize productivity, which lead to a relatively long and shallow melt pool. Consequently, the steepest thermal gradient aligns close to the build direction.^[20,42] As the underlying layer is re-melted, epitaxial growth is favored. Moreover, FCC crystals have a preferred $\langle 100 \rangle$ crystallographic growth direction. Thus, grains with preferred alignment, relative to the steepest thermal gradient, will overgrow the less favorable oriented grains.^[23,42] As a result, a columnar solidification structure is formed with primary $\langle 100 \rangle$ grains orientation aligned close to the build direction.

Figure 5(a) shows clusters of stray equiaxed/shorter grains interspersed in the columnar structure. The clusters of equiaxed grains among the columnar grain structure are recognized as stray grains. Such discrepancies could be ascribed to the direction changes of the steepest temperature gradient. As a result, the grain becomes overgrown by more favorable oriented

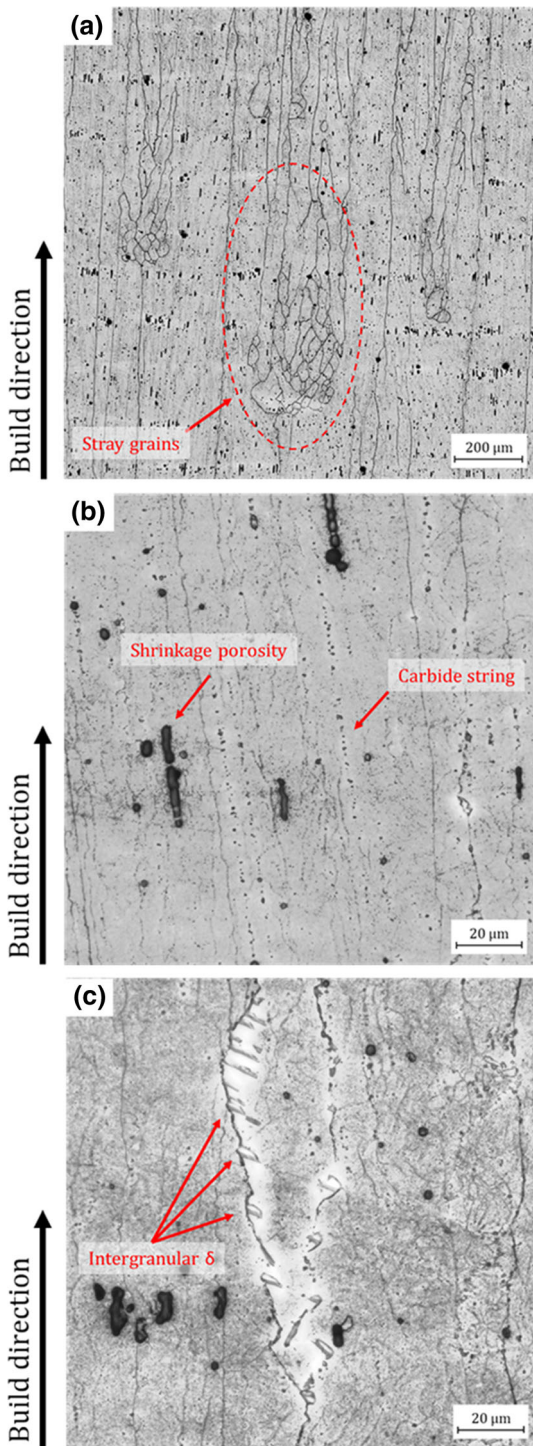


Fig. 5—Microstructure of as-built condition showing (a) columnar grain structure with stray grains, (b) shrinkage porosity and carbide strings parallel to the build direction, and (c) intergranular δ precipitates.

nuclei.^[20] A highly focused beam spot size has been shown to promote melt pool instability as temperature increases and entails higher vapor pressure.^[17] Hence, the temperature distribution along the melt pool boundary becomes inhomogeneous. Other process parameters which may associate with grain nucleation are energy input and accompanied cooling rate. If substantial microsegregation promotes constitutional undercooling, nucleation can occur at the inter dendritic front.^[43] Accordingly, the nuclei have time to grow from the melt pool border if favorable oriented before becoming overgrown.

Strings of MC precipitates could be observed in the interdendritic regions and the grain boundaries along the build direction, see Figure 5(b). Such finding is consistent with previous studies by Strondl *et al.*^[28,44] During solidification, microsegregation of elements of lower solubility in the γ matrix, such as niobium and carbon, forms primary carbides in the interdendritic liquid. These carbides accordingly become wedged into the interdendritic region during final solidification.^[45] Hence, the characteristic arrangement of the MC precipitates along the build direction.

Figure 5(c) shows precipitation of δ phase along grain boundaries. The formation of secondary phases is caused by high process temperature in conjunction with thermal cycling during fabrication. Below solidus temperature, the build starts to experience an in situ HT. Consequently, solid-state phase transformation starts, and intermetallic phases begin to precipitate.^[18] The preferred precipitation site of the δ phase is at the grain boundaries. As the δ phase is incoherent with the matrix, the grain boundaries provide a lower nucleation barrier for precipitation.^[46] Ida *et al.*^[47] studied the correlation between grain boundary orientations and δ phase precipitation in a Ni-Nb-Fe ternary alloy. Noticeably, the low angle grain boundaries ($>15^\circ$) showed a significantly lower area fraction of δ phase compared to the high angle grain boundaries. A similar observation was noticed by Deng *et al.*^[23] for EB-PBF fabricated Alloy 718. Hence, the intermittent precipitation among the grain boundaries. Furthermore, during the in situ HT, γ' and γ'' also precipitate in the matrix as the temperature drops below $\sim 900^\circ\text{C}$,^[18,21] as shown in TEM images in Figures 6(a1) through (a2).

2. Thermally Post-treated

Similar columnar grain morphology along the build direction was observed for all the HIP + STA specimens, as for the AB condition. The grains showed an average width of $73 \pm 27 \mu\text{m}$ with a height that stretched up to magnitudes of mm. The relatively narrow average grain width and the high standard deviation are attributed to the numerous narrow stray grains observed in all material conditions. No effect on the size nor the distribution of MC carbides after HT was noted. As the post-processing temperature is not sufficient for primary carbide dissolution ($\sim 1250^\circ\text{C}$)^[44], the composition and distribution of the more stable carbides stay unchanged after solidification, which is in accordance with previous studies.^[23,26]

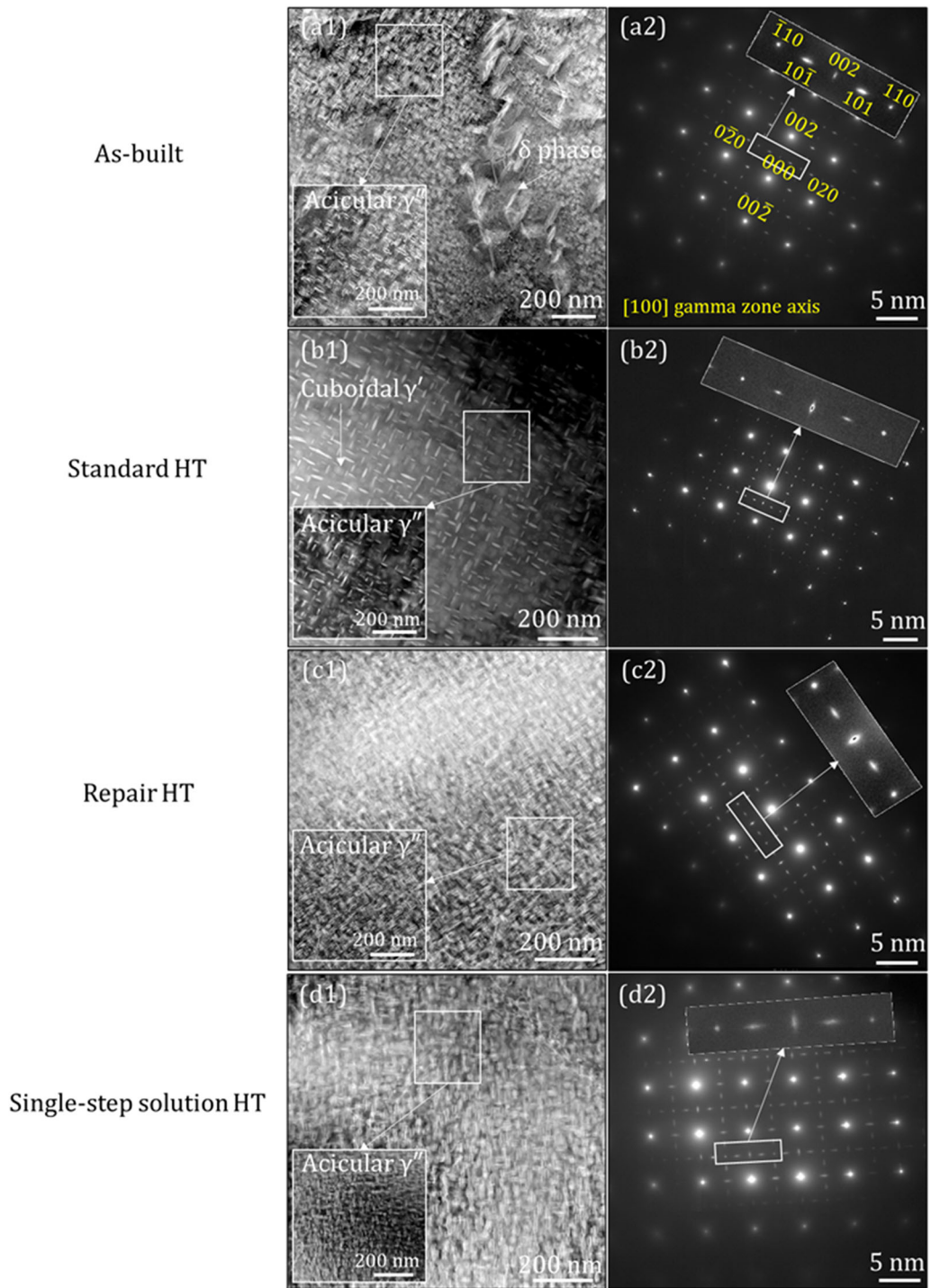


Fig. 6—Dark-field TEM images and SAD patterns of the (a1 to a2) as-built, (b1 to b2) standard, (c1 to c2) repair and (d1 to d2) single-step solution heat-treated specimens, confirming the presence of the γ'' precipitates. The δ and γ' phases were characterized in the as-built and standard HT specimens, respectively.

However, Figure 7 shows a significant difference in the size and distribution of δ precipitates among the different material conditions. The STD HT condition showed networks of intergranular precipitates and randomly distributed precipitates within the grains. Figure 7(a4) displays a grain boundary consisting of fine and densely distributed precipitates. In contrast, a

significantly coarser and more spacious distribution of δ phase is observed at the grain boundary presented in Figure 7(a5). The size and distribution variation of precipitates is assumed to correlate to the grain boundary angles. As the grain boundary energy increases with increasing grain misorientation,^[47] so does the precipitation kinetics. Therefore, δ phase primarily precipitates

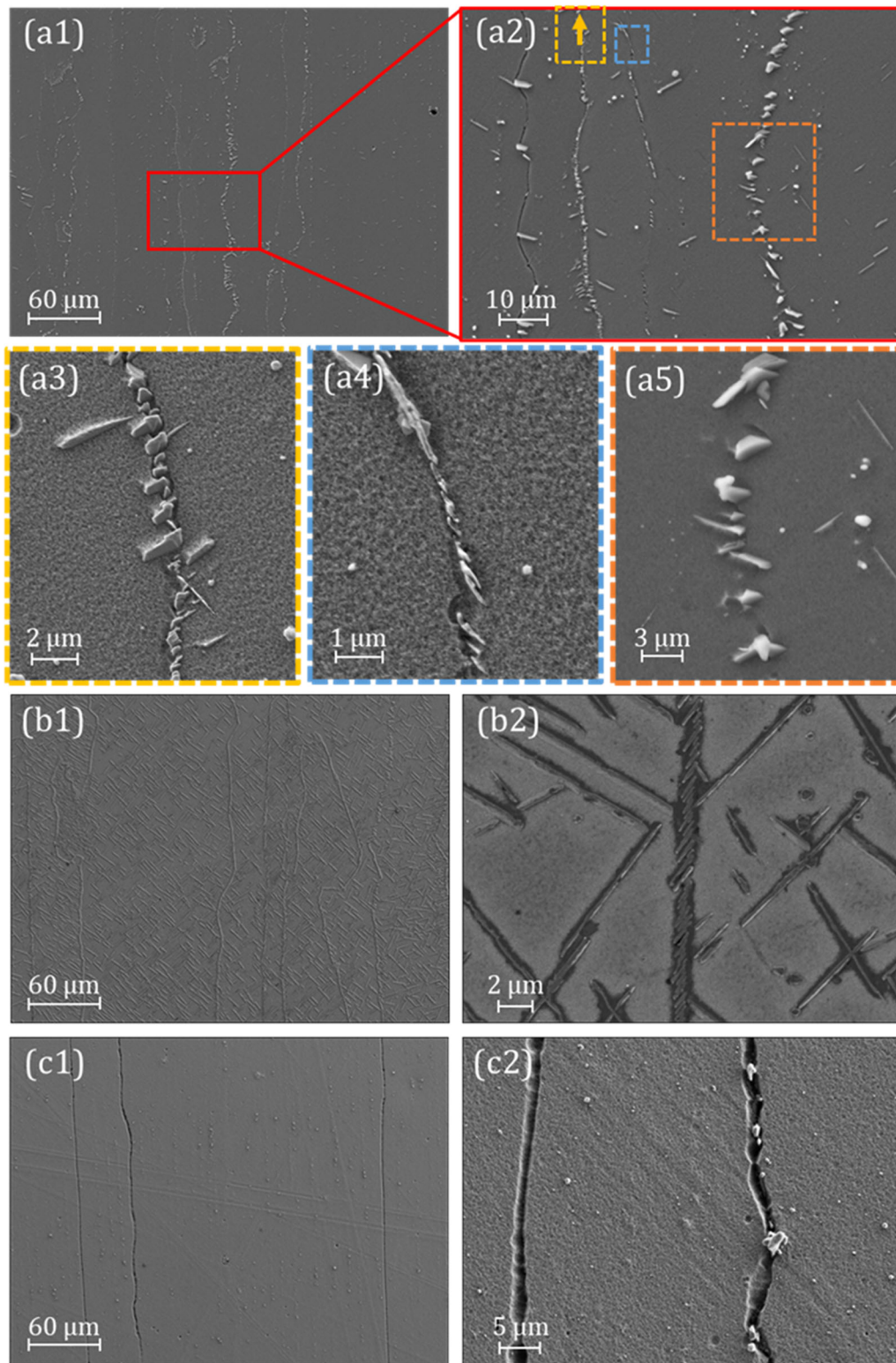


Fig. 7—SEM images showing δ phase precipitation after (a1 through a5) standard, (b1 through b2) repair, and (c1-c2) single-step solution heat treatment.

and coarsens at the high angle grain boundaries. Specimens exposed to REP HT showed a significantly higher volume fraction of intra- and intergranular δ phase precipitates due to the excessive time spent at 954

°C. Comparatively, the grain boundaries exhibited substantially denser networks of fine precipitates, see Figure 7(b2). No intragranular nor intergranular δ precipitates were observed after SSS HT. The

corresponding solution-treatment was conducted above delta solvus temperature (~ 1010 °C) and the subsequent cooling rate is too high for nucleation to occur as the temperature drops pass the precipitation windows. Furthermore, the time and temperature at the aging step are not sufficient to form δ phase. Therefore, only the carbides are observed at the grain boundaries in Figure 7(c2).

The presence of the γ'' precipitates, which were uniformly distributed in all the specimens, was confirmed using TEM, see Figure 6. The selected area diffraction (SAD) patterns were used to identify and verify the γ'' precipitates. Figures 6(a2) through (d2) shows the SAD patterns oriented along the [100] zone axis. The three post heat treatment conditions led to the formation of a regular network of acicular γ'' precipitates in the specimens. The ImageJ analysis was performed on the TEM images of the γ'' precipitates, considering that the precipitates had a disc-shaped morphology; the longer side supposed to be the diameter and shorter side supposed to be the thickness of the investigated precipitates. Comparison of the γ'' precipitate size in Table III showed that the γ'' precipitates were smaller in the sample subjected to the REP HT, whereas the difference was not apparent between the other two samples. This clearly shows the effect of Nb depletion on the formation of strengthening secondary phases due to excessive δ phase precipitation.

C. Mechanical Properties

1. First Cycle Behavior

Young's modulus (E) and yield strength (σ_y) for the material conditions were obtained by the same approach as used in.^[35] A summary of the properties is listed in Table IV. The lower E of the vertically built specimens is attributed to the strong $\langle 001 \rangle$ texture in the build direction. The inherent atomic arrangement in FCC crystals has commonly the weaker chemical bonds in the $\langle 100 \rangle$ directions, and therefore, yields lower E . Thus, crystallographic anisotropy arises as crystals align in one preferred direction. The E was approximately 35 pct higher in the horizontal orientation. The dissimilarity of moduli is in close agreement with observed anisotropy at ambient temperature in a previous study.^[35]

The STD, REP, and SSS HT showed the highest, lowest, and modest σ_y , respectively. The strength dissimilarities derive from the difference in secondary intermetallic phase precipitation. The lower σ_y of the REP conditions is attributed to the high volume of

δ -phase precipitates, causing depletion of Nb during repeated ST below δ solvus temperature. Hence, size of coherent strengthening γ'' is inhibited as was shown in Table III. The higher σ_y of the STD HT compared to the SSS HT arises from the two-stage aging treatment. Coarsening and nucleation of γ' precipitates are primarily promoted at the second aging stage.^[48] Thus, higher critical resolved shear stress is required for dislocations to shear the precipitates, and consequently, the σ_y is increased.^[49]

The transparent lines in Figure 8 present the tensile start of the first cycle for the specimens tested at 1.5 pct $\Delta\varepsilon$. Common for all specimens experiencing significant inelastic strain is the exhibited serrated plastic flow and negative strain rate sensitivity in the stress-strain curves. This phenomenon is known as the Portevin-Le Chatelier (PLC) effect, which is recognized as a subdomain of dynamic strain-aging (DSA). This behavior is associated with interactions between diffusing solute atoms and mobile dislocations.^[50,51] As temperature increases, so does diffusivity, according to Arrhenius Law. Therefore, the thermally activated PLC effect typically manifests at elevated temperatures. The diffusing solute atoms tend to interact with dislocations to lower their energy state, and accordingly, pin the dislocations from further movement. The serrations observed in this study are of type C, characterized by relatively large stress drops that occur below the general level of the flow curve, and associated with dislocation unlocking.^[50] As the dislocation is repetitively pinned and unlocked, the plastic flow becomes unstable and gives rise to the PLC effect displayed in the stress-strain curves. In addition, DSA is critically strain rate-dependent due to the competing factors of diffusivity and dislocation velocity regarding pinning and "aging" of the dislocations. Therefore, the temperature range where the PLC effect manifests will mainly depend on the strain rate and temperature. Important to note is in the cases when serrated flow was manifested before the 0.2 pct offset line in the stress-strain curve, the yield strength was estimated from the lowest stress drop prior to the offset line.

2. Cyclic Stress–Strain Curves

The cyclic stress-strain data with the corresponding fitted curve for the different material conditions are plotted in Figure 8. The curves are plotted using the true mid-life stress and strain amplitudes as representative of stable behavior and fitted by the Ramberg–Osgood relationship given by:

$$\varepsilon_a = \frac{\sigma_a}{E} + \left(\frac{\sigma_a}{H'} \right)^{n'} \quad [1]$$

where ε_a , σ_a , H' , and n' are the strain amplitude, stress amplitude, strength coefficient, and strain hardening exponent, respectively. The constants for each material condition are listed in Table V. The STD and SSS material conditions showed clear cyclic softening. However, the REP HT showed neither any significant softening nor hardening. Notably, a higher level of cyclic softening seemingly correlated to higher σ_y . This

Table III. The Size (Diameter and Thickness) of the γ'' Precipitates in the Three Samples Measured Using the ImageJ Software.

Specimen condition	Diameter (nm)	Thickness (nm)
STD	30.1 \pm 6.5	8.5 \pm 0.9
REP	20 \pm 3.8	6.8 \pm 0.4
SSS	32.3 \pm 5.9	8.9 \pm 1.1

behavior is attributed to the resistance to shearing of the strengthening intermetallic phases.^[35] The larger size, and presumably volume fraction, of the strengthening intermetallic phases in the STD and SSS conditions provide higher resistance to initial shearing in the first cycle. Thus, the shearing occurs progressively during repeated cycling. However, the smaller size of the strengthening phases in the REP conditions does not provide equal initial strengthening. Therefore, causing instant softening from the first cycle as most of the precipitates are sheared during the first peak load.

3. Cyclic stress evolution

The true stress ratio of the first and mid-life cycles was estimated to evaluate the mean stress relaxation. The stress ratio for three selected strain ranges is presented in

Table IV. Young's Modulus and Yield Strength Obtained from the Starting Tensile Cycle at 550 °C.

Specimen condition	E (GPa)	σ_y (MPa)
Vertical, STD	103 ± 7	943 ± 42
Vertical, REP	104 ± 3	667 ± 25
Vertical, SSS	108 ± 3	817 ± 9
Horizontal, STD	163 ± 11	824 ± 22
Horizontal, REP	160 ± 11	643 ± 21
Horizontal, SSS	167 ± 6	707 ± 13

Table VI. At low $\Delta\epsilon$, all material conditions showed mean tensile stress, where the vertical specimens showed complete tensile stress. All material conditions experienced increasing compressive stress at 1 pct $\Delta\epsilon$, where the horizontally oriented specimens showed substantially higher compressive stresses in comparison. For the higher $\Delta\epsilon$, all horizontally oriented specimens showed instant (or close to) symmetric stress response, whereas the vertical specimens showed further increasing compressive stresses. Notably, the STD and REP conditions showed the lowest and highest susceptibility to mean stress relaxation in all investigated $\Delta\epsilon$, respectively.

A comparison of the hysteresis loops is plotted in Figure 9. For brevity, only the SSS conditions are presented in the figure. Typically, vertical specimens tested at low $\Delta\epsilon$ presented elastic responses, whereas the horizontal specimens underwent elastic shakedown. At

Table V. Cyclic Ramberg-Osgood Constants.

Specimen condition	E (GPa)	H' (MPa)	n'
Vertical, STD	103	867	0.065
Vertical, REP	104	762	0.076
Vertical, SSS	106	780	0.064
Horizontal, STD	162	845	0.058
Horizontal, REP	160	738	0.038
Horizontal, SSS	168	764	0.068

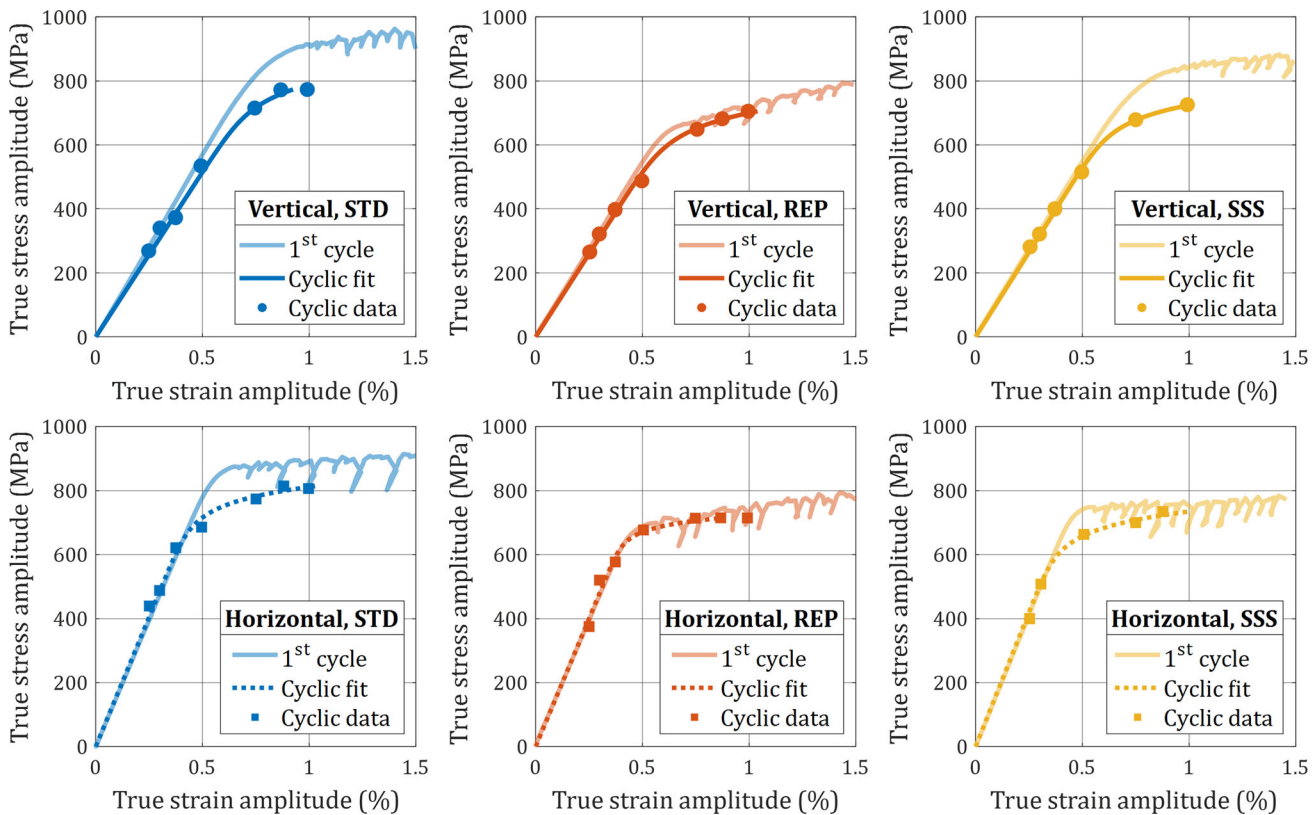


Fig. 8—Cyclic stress-strain curves fitted by the Ramberg-Osgood relationship and first cycle responses.

1 pct $\Delta\epsilon$, the horizontally oriented specimens exhibit a significant amount of cyclic plasticity. In contrast, the vertical specimens typically showed elastic shakedown, although the REP condition started to exhibit minor inelastic response. For high $\Delta\epsilon$, both tested orientations experienced cyclic plasticity. However, the vertically oriented specimens showed a substantially higher plastic response in comparison. The REP and STD HT showed the highest and lowest plastic response for a given orientation, respectively. Although, the difference is not as substantial as for the orientation-dependent response. Moreover, serrated flow was noted in all specimens showing a high degree of plastic response, as shown in the hysteresis loop in Figure 9(c). The presence of serrated flow did not seem to correlate directly to any material condition nor stress range and instead is influenced by the magnitude of plastic strain and strain rate. For the vertical specimens, serrated flow was observed at 2 pct $\Delta\epsilon$ when the plastic portion of the strain exceeded 0.4 pct. In comparison, all horizontal specimens exhibited serrated flow at 1.5 pct strain rate and above.

The cycle-dependent softening and mean stress relaxation is illustrated by the total cyclic stress evolution curves presented in Figure 10. The curves show a relatively higher stress range and lower life for all horizontal specimens. According to Hooke's law, the observed variations in the stress ranges are explained by the difference in E and the directly proportional stress-strain relationship in the elastic domain. Accordingly, higher stress evolves in the material conditions of higher E for a given strain. The specimens that experience complete elastic response or elastic shakedown exhibited saturated cyclic response, as shown in Figure 10(a). In contrast, the predominant cyclic response for material conditions experiencing a significant amount of plastic strain was cyclic softening. This behavior is manifested by a decreasing stress range and increased plastic response, as shown in Figures 9(c) and 10(c). A clear orientation-dependent difference in cyclic stress evolution can be observed in the mid $\Delta\epsilon$ as the vertical specimens show saturated cyclic response, whereas the horizontal specimens experience cyclic softening. At high $\Delta\epsilon$, all material conditions experience cyclic softening, although the cycle-dependent softening occurs more rapidly for the horizontally oriented specimens.

The phenomenon occurs due to progressive shearing of precipitates and forming of dislocation slip bands.^[52,53] With an increased number of cycles, more precipitates are sheared, and the density of the slip bands increases. Thus, the restriction of dislocation movement is reduced, and the stress range required to attain a given strain range decreases. The influence of elevated temperature on the cyclic response has previously been studied for wrought Alloy 718 and shows consistent results for analogous temperatures.^[52,54]

4. Strain-life relationship

The total strain-life relationship for all the material conditions is presented in Figure 11. The ϵ_a - N curves are

fitted by superposition of the elastic (ϵ_a^{el}) and plastic (ϵ_a^{pl}) parts of the total strain amplitude (ϵ_a) expressed as:

$$\epsilon_a = \epsilon_a^{\text{pl}} + \epsilon_a^{\text{el}} \quad [2]$$

where ϵ_a^{el} is derived from the mid-life stress amplitude and E according to Hooke's law given by:

$$\epsilon_a^{\text{el}} = \frac{\sigma_a}{E} = A(N_f)^z \quad [3]$$

and ϵ_a^{pl} is the difference between ϵ_a and ϵ_a^{el} given by:

$$\epsilon_a^{\text{pl}} = B(N_f)^\beta \quad [4]$$

The linear plastic and elastic ϵ_a - N relationships were fitted following ASTM E739.^[55] Where coefficients and exponents for respective material conditions are listed in Table VII.

In general, the fatigue life for all material conditions was increased with decreasing strain amplitude as expected. Virtually no disparity in total life could be observed for the different HT conditions. However, a noticeable increase in life could be observed for the vertically oriented specimens, which showed on average $\sim 5\times$ greater life in comparison to the horizontally oriented specimens. Similar orientation-dependent fatigue life has been reported by Kirka *et al.*^[34] and Balachandramurthi *et al.*^[35] Consistent with the mentioned studies, the difference in life can be attributed to the crystallographic texture-dependent modulus and resulting stress evolution. Hence, the higher E of the horizontal originated specimens induces a higher plastic response and consequently reduced fatigue life. Balachandramurthi *et al.*^[35] showed the relationship of strain and crystallographic orientation by plotting the pseudo-elastic stress versus life in a log-log plot, where the pseudo-elastic stress is given by:

$$\sigma_{\text{pseudo-elastic}} = \epsilon_a \times E \quad [5]$$

A comparison of the strain amplitude and pseudo-elastic stress is presented in Figure 12 by implementing the above approach. As shown in Figure 12(b), the scatter between the orientations is reduced, and the data points merge into a more linear trend. Thus, a verification of the assumption that texture influences fatigue life. Additionally, room temperature data from^[35] is plotted in Figure 12. In comparison, higher life was noted at low ϵ_a for specimens tested at elevated temperature and the opposite behavior was observed at high ϵ_a . These findings contradict reported quasistatic tensile behavior,^[21,22] where the monotonic tensile strength being unanimously lower at higher homologous temperatures. Similar increase in life at low ϵ_a and high temperature has been reported from wrought^[56] and AM fabricated^[57,58] Alloy 718. This deviating behavior can be attributed to the formation of oxide films on the free surface. The growth of oxide film impedes the formation of slip band-induced extrusions and intrusions at the surface, which consequently

Table VI. Comparison of First Cycle and Mid-life Stress Ratio.

Specimen condition	$\Delta\varepsilon = 0.6\%$		$\Delta\varepsilon = 1\%$		$\Delta\varepsilon = 1.5\%$	
	1st	N/2	1st	N/2	1st	N/2
Vertical, STD	0.00	0.00	- 0.20	- 0.21	- 0.68	- 0.75
Vertical, REP	- 0.02	- 0.08	- 0.31	- 0.39	- 0.63	- 0.76
Vertical, SSS	- 0.01	- 0.04	- 0.23	- 0.26	- 0.70	- 0.78
Horizontal, STD	- 0.14	- 0.15	- 0.65	- 0.72	- 0.98	- 0.99
Horizontal, REP	- 0.39	- 0.51	- 0.79	- 0.93	- 0.90	- 0.95
Horizontal, SSS	- 0.34	- 0.40	- 0.92	- 0.96	- 1.05	- 1.05

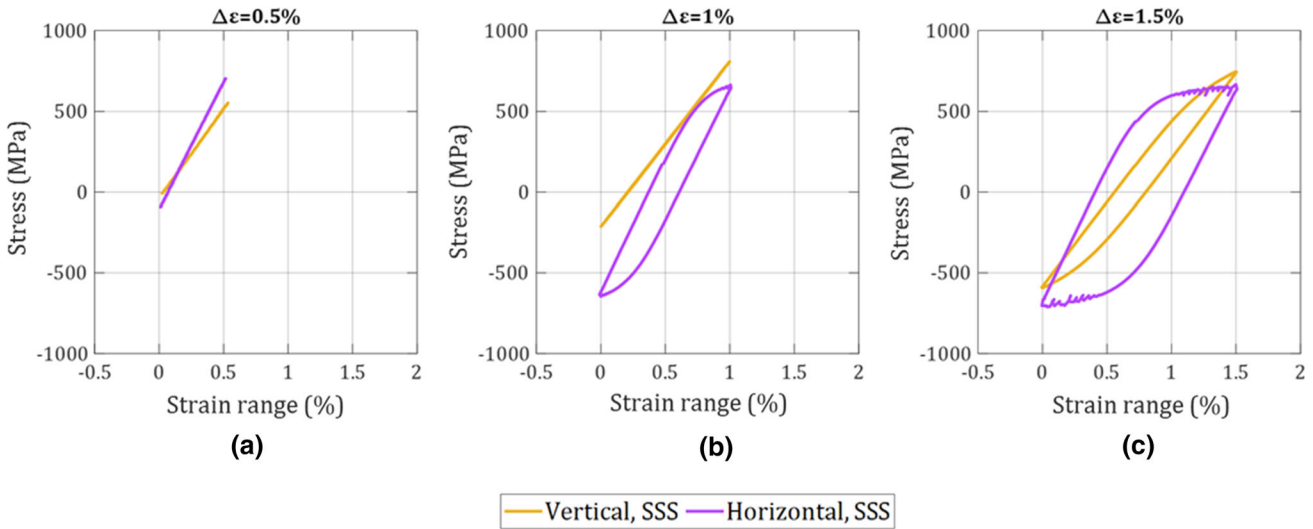


Fig. 9—Mid-life hysteresis loops for specimens in SSS condition at (a) 0.5 pct, (b) 1 pct, and (c) 1.5 pct strain range.

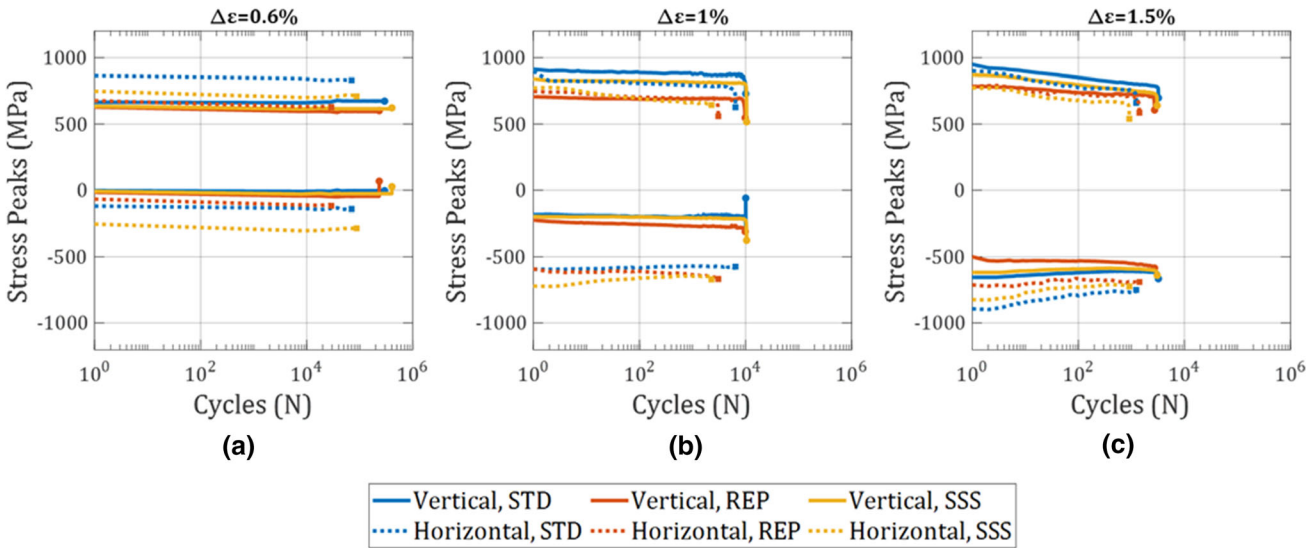


Fig. 10—Cyclic stress evolution curves for specimens tested at (a) 0.6 pct, (b) 1 pct, and (c) 1.5 pct strain range.

inhibits crack nucleation. However, at higher ε_a , the oxide layer is not sufficient to endure the enhanced slipping due to the higher stress. The grey dashed line in Figure 12(b) indicates the critical pseudo-elastic stress

where a significant shift in the number of cycles to failure occurs in Figure 12(a). Moreover, the mechanism of competing failure modes may have influenced the fatigue performance, which will be further discussed in

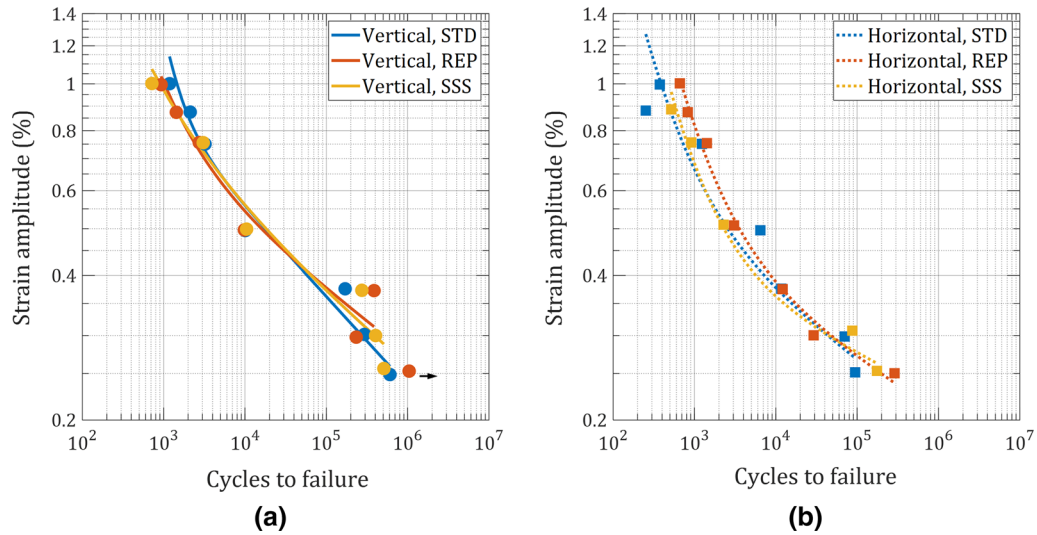


Fig. 11—Strain amplitude-life plots with fitted curves for the different material conditions. The black arrow represents specimen who reached the run-out limit.

Table VII. Constants and Exponents for Strain-Life Relationship Curve Fits.

Specimen Condition	Elastic part		Plastic part	
	A (Pct)	α (-)	B (Pct)	β (-)
Vertical, STD	3.07	- 0.19	4.4×10^5	- 2.00
Vertical, REP	1.71	- 0.13	188	- 0.92
Vertical, SSS	1.98	- 0.15	31	- 0.69
Horizontal, STD	1.18	- 0.13	146	- 0.97
Horizontal, REP	1.00	- 0.11	290	- 0.97
Horizontal, SSS	0.74	- 0.09	259	- 0.99

section 3.4. However, these findings need to be interpreted with caution as randomness in inclusion distribution may have been unfavorable and influenced the result. In summary, at high ϵ_a , high-temperature specimens exhibit lower life due to material softening and oxidation-assisted initiation and crack propagation.^[59] At lower ϵ_a , the formation of stable oxide films on the free surface under the high-temperature condition may aid to inhibits surface slip.

D. Fractography

Investigation of the post-mortem surfaces showed crack initiation at one or several sites caused from one of the following crack initiation modes:

- I. Planar slip bands at the free surface.
- II. Surface-connected inclusions.
- III. Internal inclusions.
- IV. Combination of initiation sites I and II.

Representative crack initiation modes are presented in Figure 13. Surface-connected inclusions refer to inclusions located within the distance of the inclusion diameter from the free surface. Each type of initiation mode for the specific specimen is presented in Figure 12.

Initiation mode I, II, and III is represented by filled, unfilled, and unfilled with point markers, respectively. Two specimens exhibiting type IV initiation are represented in an equal manner as type II for brevity. Note that fracture surfaces of specimens marked with red color crosses were not investigated as those specimens were preserved for crack propagation investigation.

Figure 12(a) shows that the majority of the specimens exhibiting superior life compared to the room temperature data also presented internal crack initiation. Notably, foremost internal crack initiation was observed at lower stress levels, see Figure 12(b). The seeming correlation between crack initiation location and ϵ_a is interesting because previous studies at ambient temperature have reported solely crack initiation near the surface for corresponding ϵ_a .^[30,35] However, competitive failure modes have previously been reported in high strength alloys at elevated temperatures.^[60] The competing failure modes are evident in the current study as dual failure distributions are observed at 0.375 pct ϵ_a in Figure 12(a). While a similar change of initiation site was noticed for LB-PBF fabricated Ni-based GH4169 superalloy at 650 °C, little influence on fatigue performance was found compared to room temperature testing.^[61] Comparatively, the current study showed enhanced fatigue life for the EB-PBF Alloy 718 related to the initiation mode transition. Important to note at elevated temperatures is an absence of oxidation-assisted crack growth when cracks do not propagate from the surface.^[60] Thus, the crack growth rate is lower, and consequently, fatigue life is prolonged.

The transition from surface to internal initiation at low stress is attributed to a more homogeneous dislocation structure at elevated temperatures.^[62] As plastic localization decreases, strain accumulation due to a lower degree of constraints at the surface becomes less pronounced. Hence, the highest stress becomes localized at the most detrimental defect regarding size, morphology and orientation, and less dependent on the

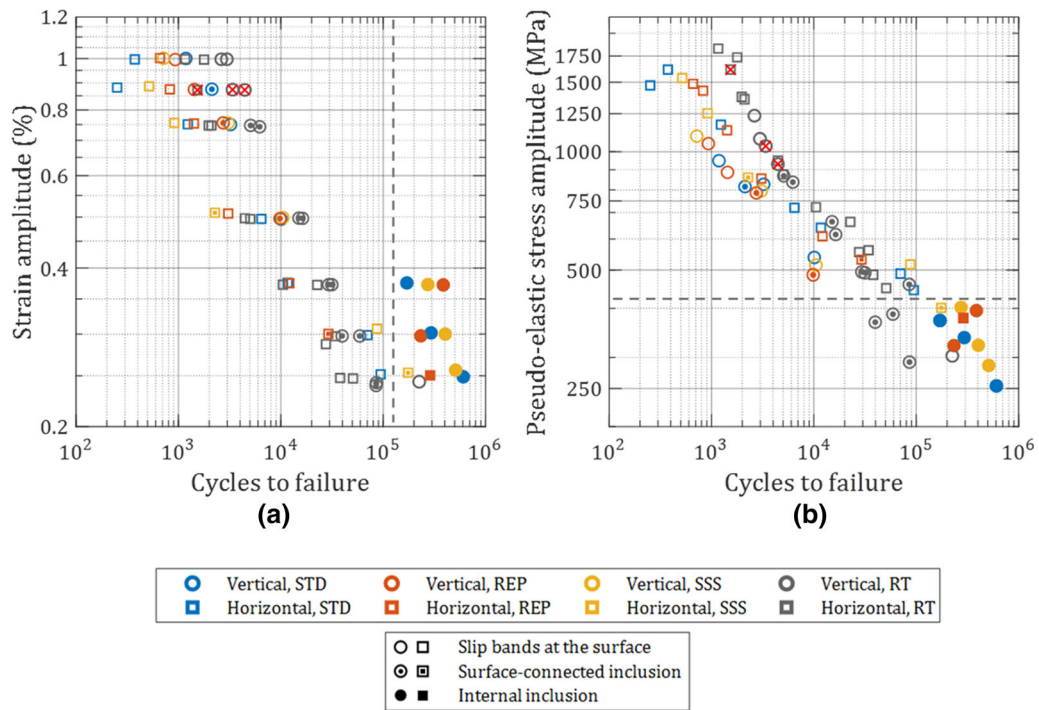


Fig. 12—(a) Stress amplitude-life and (b) pseudo-elastic stress-life plots. Filled, unfilled, and unfilled with point markers represent crack initiation from internal inclusion, slip bands at the surface, and inclusion at the surface, respectively. Fracture surfaces of red crossed markers were not investigated. The grey dashed line represents (a) the number of cycles where fatigue life is significantly increased and (b) the corresponding pseudo-elastic stress. Room temperature (RT) data are obtained from Ref. 35 (Color figure online).

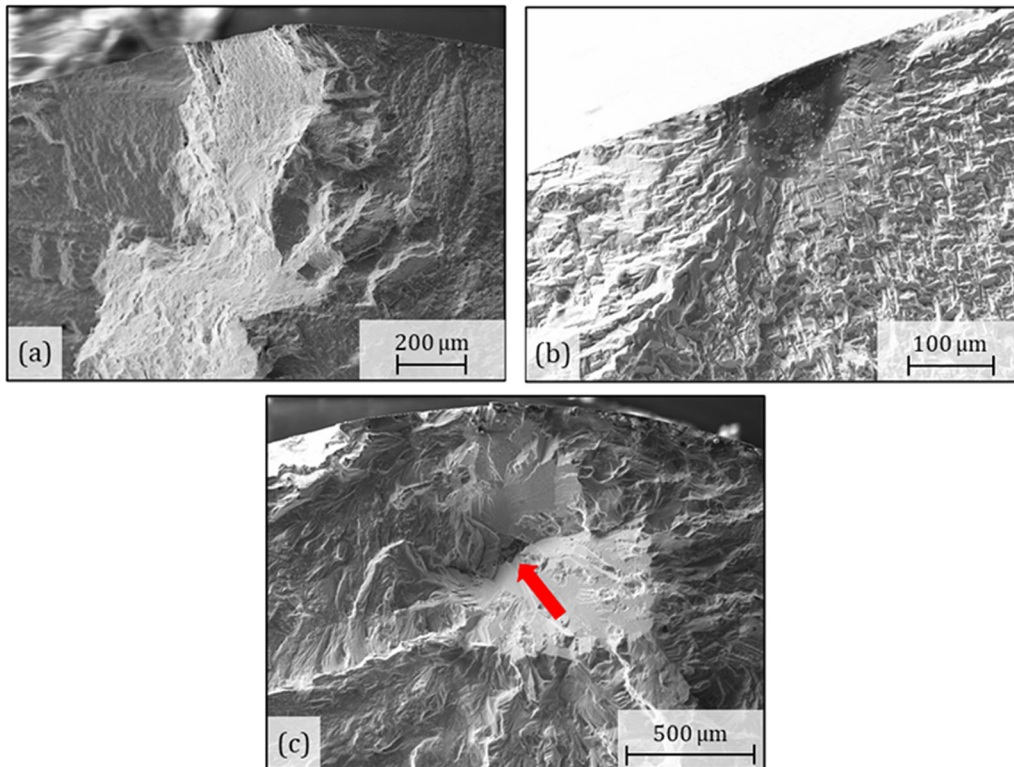


Fig. 13—Crack initiation sites. Crack initiation from (a) planar slip bands at the surface, (b) surface connected non-metal inclusion, and (c) internal non-metal inclusion.

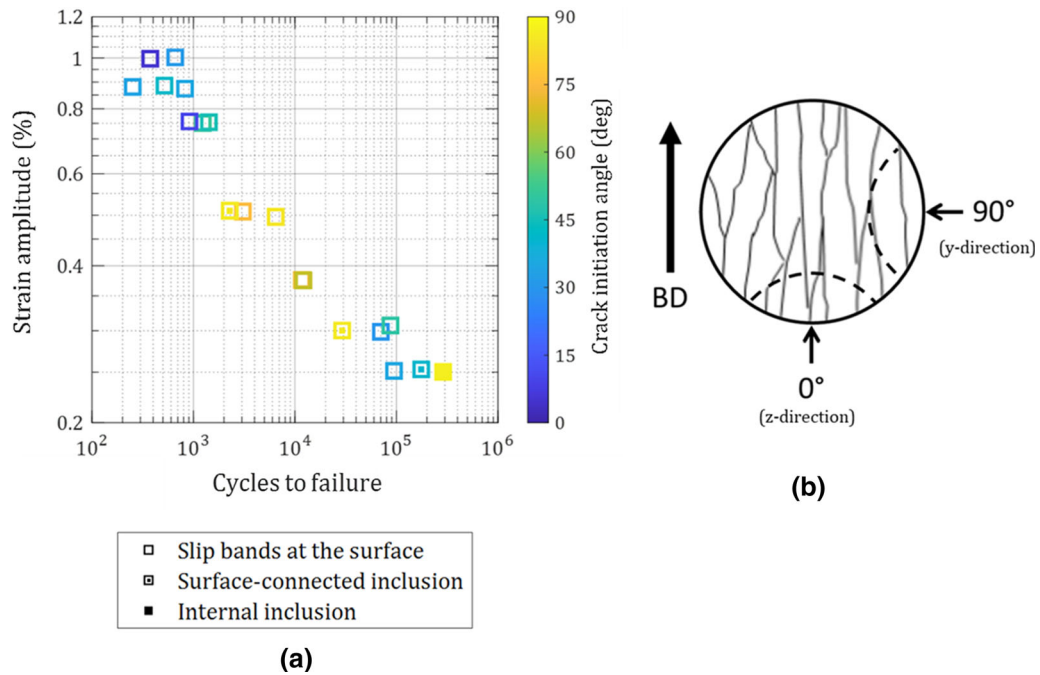


Fig. 14—(a) Stress amplitude-life plot for horizontally orientated specimens with a color bar representing the crack initiation site with respect to the grain alignment. (b) Schematic representation of parallel and perpendicular crack initiation relative to the columnar grain alignment (Color figure online).

location.^[63] As the bulk volume significantly exceeds the surface volume, so does the probability that the most detrimental defect is located internally. Consequently, cracks will most likely initiate from an internal defect under circumstances where the surface does not accumulate a significant amount of plastic strain.

E. Crack Initiation Angle

The same data points for the horizontal specimens presented in Figure 12 have been re-plotted in Figure 14(a). The color bar in Figure 14 represents the initiation angle relative to the elongated grain orientation (z -direction), as schematically illustrated in Figure 14(b). Accordingly, dark-blue markers represent horizontal specimens with crack initiation sites close to 6 or 12 o'clock position relative to the build direction. In a similar manner, the light-yellow markers represent horizontal specimens with crack initiation close to 3 or 9 o'clock position. Furthermore, a comparison of the fracture surfaces at high and low ε_a with different initiation angles is presented in Figure 15. A previous study has investigated the dwell-fatigue crack propagation parallel (z -direction) and perpendicular (x -direction) to the build direction in notched specimens.^[33] It was shown that the crack propagation rate was significantly higher in the z -direction compared to x -directions. In the current study, an attempt to compare the crack initiation between the z - and y -direction has been

established. Excluding mode II failure, the initiation angles close to parallel (z -direction) and perpendicular (y -direction) to the columnar grains exhibited the lowest and highest life for the given strain range, respectively. Thus, an indication that the initiation angle might influence fatigue performance. Although cracks might initiate around approximately the same number of cycles, the number of cycles spent in propagation mode might be significantly different depending on the initiation site. However, given that our findings are based on a limited number of data points, the results should be treated with considerable caution. Therefore, future crack propagation studies are required to evaluate the influence of grain orientation on crack growth.

IV. CONCLUSIONS

In this work, the fatigue behavior at 550 °C of EB-PBF fabricated Alloy 718 was studied. Three different heat treatment routes were investigated in two different orientations with respect to the build direction under strain-controlled conditions. The main conclusions from this work are:

- Alloy 718 exhibits dynamic strain aging by manifestation of serrated flow in the plastic region of the hysteresis loops for the given temperature and strain rates.

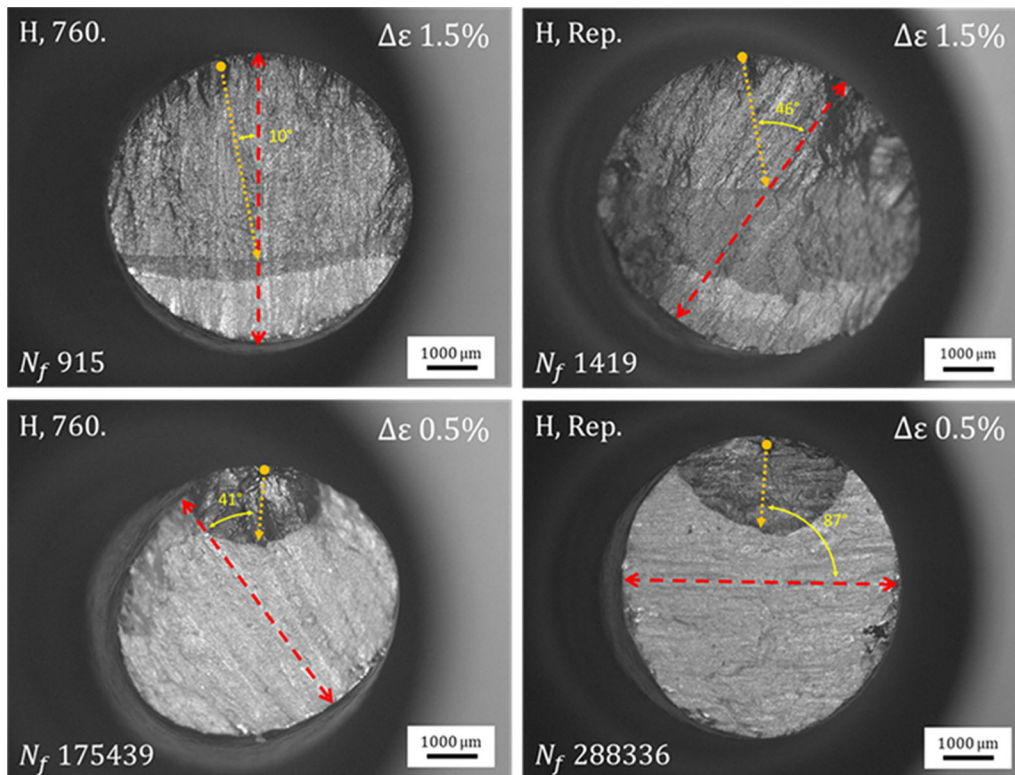


Fig. 15—Fracture surfaces with crack propagation front with respect to the grain alignment. The orange-dotted arrows represent crack initiation site and propagation until failure. The red-dashed arrows represent the elongated direction of the columnar grains. The lightest grey region of the fracture surface corresponds to the final fracture area (Color figure online).

- The grain orientation has a significant influence on the cyclic stress evolution and the total fatigue life due to the crystallographic texture-induced anisotropy.
- The volume fraction of δ phase precipitates has no significant effect on the total fatigue life in the scope of this study.
- Crack initiation location shifts between internal and surface initiation depending on the resolved shear stress acting on the slip plane at elevated temperature independent of the heat treatment condition.
- Fatigue life at 550 °C is lower at high strain amplitudes but higher at low strain amplitudes compared to fatigue life at room temperature.

ACKNOWLEDGMENTS

This study was founded by the KK foundation through the SUMAN Next project (20160281). The authors would like to acknowledge Jonas Olsson for helping with manufacturing EB-PBF specimens. The authors would also like to thank Mats Högström and Håkan Backström for their help with setting up and performing the LCF tests. The authors are also grateful to Dr. Esmail Sadeghi for preparing and providing the TEM images.

CONFLICT OF INTEREST

On behalf of all authors, the corresponding author states that there is no conflict of interest.

FUNDING

Open access funding provided by University West.

OPEN ACCESS

This article is licensed under a Creative Commons Attribution 4.0 International License, which permits use, sharing, adaptation, distribution and reproduction in any medium or format, as long as you give appropriate credit to the original author(s) and the source, provide a link to the Creative Commons licence, and indicate if changes were made. The images or other third party material in this article are included in the article's Creative Commons licence, unless indicated otherwise in a credit line to the material. If material is not included in the article's Creative Commons licence and your intended use is not permitted by statutory regulation or exceeds the permitted use, you will need to obtain permission directly from the copyright holder. To view a copy of this licence, visit <http://creativecommons.org/licenses/by/4.0/>.

ABBREVIATIONS

$\Delta\varepsilon$	Strain range
δ	Delta phase
E	Young's modulus
ε_a	Strain amplitude
γ'	Gamma prime phase
γ''	Gamma double prime phase
H'	Strength coefficient
n'	Strain hardening exponent
N	Number of cycles
N_f	Number of cycles to failure
σ_a	Stress amplitude
σ_y	Yield strength

REFERENCES

- C.K. Chua and K.F. Leong: in *3D Print. Addit. Manuf.*, 5th ed., World Scientific Publishing Company, Hackensack, NJ, 2017, pp. 137–96.
- A. Saboori, A. Aversa, G. Marchese, S. Biamino, M. Lombardi, and P. Fino: *Appl. Sci.*, 2019, vol. 9, p. 3316.
- V. Bhavar, P. Kattire, V. Patil, S. Khot, K. Gujar, and R. Singh: in *Addit. Manuf. Handb.*, A.B. Badiru, V.V. Valencia, and D. Liu, eds., 1st ed., CRC Press, Boca Raton, FL, 2017, pp. 251–53.
- A. Salmi, F. Calignano, M. Galati, and E. Atzeni: *Virtual Phys. Prototype.*, 2018, vol. 13, pp. 191–202.
- L.J. Kumar and C.G. Krishnadas Nair: in *Adv. 3D Print. Addit. Manuf. Technol.*, D.I. Wimpenny and P.M. Pandey, eds., 1st Edn. Springer, Singapore, 2017, pp. 39–54.
- E. Hosseini and V.A. Popovich: *Addit. Manuf.*, 2019, vol. 30, p. 100877.
- M.J. Donachie and S.J. Donachie: in *Superalloys Tech. Guide*, 2nd ed., ASM International, Materials Park, OH, 2002, pp. 1–9.
- E.E. Brown and D.R. Muzyrka: in *Superalloys II*, C.T. Sims, N.S. Stoloff, and W.C. Hagel, eds., John Wiley & Sons, Inc., Hoboken, NJ, 1987, pp. 165–88.
- G. Sjöberg, N. Ingesten, and R.G. Carlson: *Superalloys*, 1991, pp. 603–20.
- B. Geddes, X. Huang, and H. Leon: in *Superalloys Alloy. Perform.*, 1st ed., ASM International, Materials Park, OH, 2010, pp. 25–57.
- N. El-Bagoury, T. Matsuba, K. Yamamoto, H. Miyahara, and K. Ogi: *Mater. Trans.*, 2005, vol. 46, pp. 2478–83.
- M.A. Xavier, M. Manohar, P. Jeyapandiarajan, and P.M. Madhukar: *Procedia Eng.*, 2017, vol. 174, pp. 1000–1008.
- GE Additive: n.d.
- J. Kruth, S. Dadbakhsh, B. Vrancken, K. Kempen, J. Vleugels, and J. Humbeeck: in *Addit. Manuf. Innov. Adv. Appl.*, T.S. Srivatsan and T.S. Sudarshan, eds., 1st ed., CRC Press, Boca Raton, FL, 2016, pp. 70–96.
- R.M. Mahamood and E.T. Akinlabi: in *Adv. Mater. Sci. Res.*, M.C. Wythers, ed., Nova Science Publishers, Inc, New York, NY, 2017, pp. 8–11.
- C. Körner: *Int. Mater. Rev.*, 2016, vol. 61, pp. 361–77.
- H. Helmer, C. Körner, and R.F. Singer: *J. Mater. Res.*, 2014, vol. 29, pp. 1987–96.
- W.J. Sames, K.A. Unocic, R.R. Dehoff, T. Lolla, and S.S. Babu: *J. Mater. Res.*, 2014, vol. 29, pp. 1920–30.
- W.J. Sames: Doctoral dissertation, Texas A & M University, 2015.
- H. Helmer, A. Bauereiß, R.F. Singer, and C. Körner: *Mater. Sci. Eng. A.*, 2016, vol. 668, pp. 180–87.
- M.M. Kirka, K.A. Unocic, N. Raghavan, F. Medina, R.R. Dehoff, and S.S. Babu: *JOM.*, 2016, vol. 68, pp. 1012–20.
- M.M. Kirka, Y. Lee, D.A. Greeley, A. Okello, M.J. Goin, M.T. Pearce, and R.R. Dehoff: *JOM.*, 2017, vol. 69, pp. 523–31.
- D. Deng, J. Moverare, R.L. Peng, and H. Söderberg: *Mater. Sci. Eng. A.*, 2017, vol. 693, pp. 151–63.
- P. Karimi: PhD Thesis, University West, 2020.
- M.M. Kirka, F. Medina, R. Dehoff, and A. Okello: *Mater. Sci. Eng. A.*, 2017, vol. 680, pp. 338–46.
- A.R. Balachandramurthi, J. Moverare, S. Mahade, and R. Pederson: *Materials.*, 2018, vol. 12, p. 68.
- D. Kotzem, P. Dumke, P. Sepehri, J. Tenkamp, and F. Walther: *Prog. Addit. Manuf.*, 2020, vol. 5, pp. 267–76.
- A. Strondl, M. Palm, J. Gnauk, and G. Frommeyer: *Mater. Sci. Technol.*, 2011, vol. 27, pp. 876–83.
- K. Unocic, L. Kolbus, R. Dehoff, S. Dryepondt, and B. Pint: in *Corros.* 2014, San Antonio, TX, 2014.
- E. Sadeghi, P. Karimi, N. Israelsson, J. Shipley, T. Månsson, and T. Hansson: *Addit. Manuf.*, 2020, vol. 36, p. 101670.
- A.R. Balachandramurthi, J. Moverare, N. Dixit, D. Deng, and R. Pederson: *Mater. Charact.*, 2019, vol. 149, pp. 82–94.
- A.R. Balachandramurthi, J. Moverare, N. Dixit, and R. Pederson: *Mater. Sci. Eng. A.*, 2018, vol. 735, pp. 463–74.
- D. Deng, R.L. Peng, and J. Moverare: *Mater. Sci. Eng. A.*, 2019, vol. 760, pp. 448–57.
- M.M. Kirka, D.A. Greeley, C. Hawkins, and R.R. Dehoff: *Int. J. Fatigue.*, 2017, vol. 105, pp. 235–43.
- A.R. Balachandramurthi, J. Moverare, T. Hansson, and R. Pederson: *Int. J. Fatigue.*, 2020, vol. 141, p. 105898.
- ASTM Standard F3055 - 14a, ASTM International, West Conshohocken, PA, 2014.
- ASTM Standard E606/E606M - 12, ASTM International, West Conshohocken, PA, 2012.
- D. Deng, R.L. Peng, H. Söderberg, and J. Moverare: *Mater. Des.*, 2018, vol. 160, pp. 251–61.
- G. Chen, S.Y. Zhao, P. Tan, J. Wang, C.S. Xiang, and H.P. Tang: *Powder Technol.*, 2018, vol. 333, pp. 38–46.
- S. Tammam-Williams, P.J. Withers, I. Todd, and P.B. Prangnell: *Scr. Mater.*, 2016, vol. 122, pp. 72–76.
- R. Cunningham, A. Nicolas, J. Madsen, E. Fodran, E. Anagnostou, M.D. Sangid, and A.D. Rollett: *Mater. Res. Lett.*, 2017, vol. 5, pp. 516–25.
- A.A. Antonysamy, J. Meyer, and P.B. Prangnell: *Mater. Charact.*, 2013, vol. 84, pp. 153–68.
- A.M. Rausch, M.R. Gotterbarm, J. Pistor, M. Markl, and C. Körner: *Materials.*, 2020, vol. 13, p. 5517.
- A. Strondl, R. Fischer, G. Frommeyer, and A. Schneider: *Mater. Sci. Eng. A.*, 2008, vol. 480, pp. 138–47.
- M.C. Flemings: *Metall. Trans.*, 1974, vol. 5, pp. 2121–34.
- M. Sundararaman, P. Mukhopadhyay, and S. Banerjee: *Metall. Trans. A.*, 1988, vol. 19, pp. 453–65.
- S. Ida, S. Kobayashi, and M. Takeyama: *J. Alloys Compd.*, 2018, vol. 764, pp. 1033–38.
- H.-Y. Bor, Chao-Nan Wei, H.T. Nguyen, An-Chou Yeh, and C.-M. Kuo: in *Superalloy 718 Deriv.*, E. Ott, J. Groh, A. Banik, I. Dempster, T. Gabb, R. Helmink, X. Liu, A. Mitchell, G. Sjöberg, and A. Wusatowska-Sarneck, eds., Wiley, 2010, pp. 678–88.
- N.S. Stoloff: in *Superalloys II*, C.T. Sims and W.C. Hagel, eds., John Wiley & Sons, Inc., Hoboken, NJ, 1987, pp. 61–96.
- P. Rodriguez: *Bull. Mater. Sci.*, 1984, vol. 6, pp. 653–63.
- S.L. Mannan: *Bull. Mater. Sci.*, 1993, vol. 16, pp. 561–82.
- D. Fournier and A. Pineau: *Metall. Trans. A.*, 1977, vol. 8, pp. 1095–105.
- L. Xiao, D.L. Chen, and M.C. Chaturvedi: *Scr. Mater.*, 2005, vol. 52, pp. 603–07.
- H.F. Merrick: *Metall. Trans.*, 1974, vol. 5, pp. 891–97.
- ASTM Standard E739 - 10, ASTM International, West Conshohocken, PA, 2015.
- Q. Kawagoishi, D. Chen, and G. Nisitani: *Fatigue Fract. Eng. Mater. Struct.*, 2000, vol. 23, pp. 209–16.
- S. Gribbin, S. Ghorbanpour, N.C. Ferreri, J. Bicknell, I. Tsukrov, and M. Knezevic: *Mater. Charact.*, 2019, vol. 149, pp. 184–97.
- P.D. Nezhadfar, A.S. Johnson, and N. Shamsaei: *Int. J. Fatigue.*, 2020, vol. 136, p. 105598.
- D. Gustafsson, J. Moverare, S. Johansson, M. Hörnqvist, K. Simonsson, S. Sjöström, and B. Sharifimajda: *Procedia Eng.*, 2010, vol. 2, pp. 1095–1104.
- G.T. Cashman: *Int. J. Fatigue.*, 2010, vol. 32, pp. 492–96.

61. W. Li, R. Sun, T. Hu, X. Li, C. Li, Y. Zhang, X. Ding, and P. Wang: *Int. J. Fatigue.*, 2021, vol. 148, p. 106250.
62. J.C. Stinville, E. Martin, M. Karadge, S. Ismonov, M. Soare, T. Hanlon, S. Sundaram, M.P. Echlin, P.G. Callahan, W.C. Lenthe, V.M. Miller, J. Miao, A.E. Wessman, R. Finlay, A. Loghin, J. Marte, and T.M. Pollock: *Acta Mater.*, 2018, vol. 152, pp. 16–33.
63. G.T. Cashman: *J. Eng. Mater. Technol.*, 2007, vol. 129, pp. 293–303.

Publisher's Note Springer Nature remains neutral with regard to jurisdictional claims in published maps and institutional affiliations.